ACS APPLIED ENERGY MATERIALS

www.acsaem.org Article

Bifunctional Water Splitting Photoelectrocatalysts Using Flexible Organometallic Complex and Nanographene Multilayer Thin Films

Dongseok Kim, Minsu Gu,* Yeongkyu Choi, Hyunwoo Kim, Jungki Ryu, and Byeong-Su Kim*

Cite This: https://dx.doi.org/10.1021/acsaem.0c01154 Read Online

ACCESS | Metrics & More | Article Recommendations | Supporting Information

ABSTRACT: In comparison with conventional inorganic photocatalysts, organic photoactive materials are promising photocatalysts owing to their high extinction coefficient and chemical tunability. However, their limited photocatalytic activity, induced by a low relative permittivity with high recombination energy, poses significant challenges. Herein, a highly efficient bifunctional photocatalytic hybrid multilayer electrode is designed by a versatile layer-by-layer (LbL) assembly of nanoscale graphene oxide (nGO) and a ruthenium−terpyridine coordination complex (TPY_2Ru). We exploited a synergistic effect between two active components, namely, the generation of photoinduced excitons by TPY_2Ru and the facilitation of electron transfer by reducing the recombination rate of the generated electrons by nGO in hybrid electrodes. This photocatalytic electrode exhibits bifunctional activities for water splitting in neutral condition with the highest photoanodic current density of 4.28 $\mu A/cm^2$ at 1.23 V versus a reversible hydrogen electrode (RHE) and a photocathodic current density of 28.42 $\mu A/cm^2$ at 0 V versus RHE. Furthermore, the unique combination of hybrid materials enables the development of flexible photocatalytic electrodes with remarkable current density retention after a 1000-cycle durability test. Because of the highly tunable properties of the LbL-assembled multilayer electrodes, we anticipate that this strategy can offer insights into the nanoscale-architecture-controlled engineering of efficient photoelectrodes for future solar-fuel energy devices.

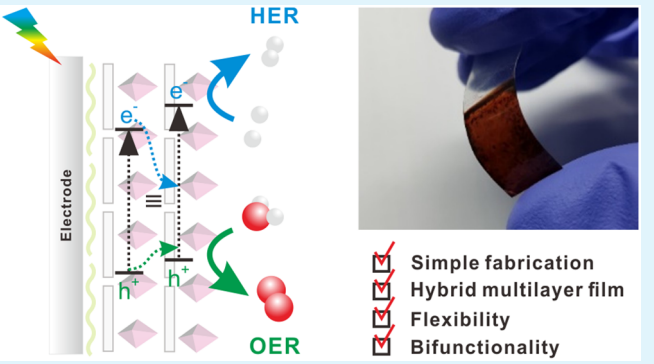

KEYWORDS: *photoelectrocatalysts, oxygen evolution reaction, hydrogen evolution reaction, bifunctionality, layer-by-layer assembly*

INTRODUCTION

Solar energy conversion has long been considered one of the most promising strategies for sustainable-energy and fuel productions to overcome the challenges of an impending global energy crisis resulting from the depletion of fossil fuels.[1−3] Photoelectrochemical (PEC) water splitting is a representative example that allows the production of pure hydrogen fuel, without any pollutants, through direct solar-to-chemical conversion—the so-called artificial photosynthesis.[4−8] Consequently, efficient and cost-effective photocatalysts are required for both oxygen evolution reaction (OER) and hydrogen evolution reaction (HER).[9] Significant progress has been made in the development of various inorganic photocatalysts using noble metals, semiconducting metal oxides, chalcogenide nanoparticles, quantum dots, and nanocomposites.[10,11] However, the intrinsic drawbacks of inorganic materials, including low processability, low extinction coefficient, and improper band structure, have limited efficient solar-to-chemical conversion. Moreover, bifunctional photoelectrodes have been rarely reported despite the several practical benefits primarily because the band-edge position of most inorganic semiconductors only satisfies one of the half-reactions in overall water splitting (i.e., HER or OER).[12]

Defective nanocarbons, such as graphene oxide, graphene quantum dots, and carbon nanodots, have received intensive attention in various fields because of their superior physical and electrical properties.[13−15] In particular, nanoscale sp^2-graphitic structures in photocatalysts is promising for water splitting reactions, possessing outstanding light-harvesting characteristics owing to a band gap for the $\pi-\pi^*$ transition and the quantum confinement effect.[16−19] As a representative example by Teng and co-workers, the electronic structures of p-type graphene oxide were tailored to the n-type by nitrogen doping for HER.[16,17] Overall water splitting was also achieved by building an interfacial junction between nondoped and nitrogen-doped graphene oxide quantum dots. However, individual photocatalytic carbon-based materials exhibit the critical limitations of a high recombination rate of electron/hole pairs and a difficulty in the fabrication process of

Received: May 19, 2020
Accepted: June 30, 2020
Published: June 30, 2020

https://dx.doi.org/10.1021/acsaem.0c01154
ACS Appl. Energy Mater. XXXX, XXX, XXX−XXX

Scheme 1. Schematic Illustration of LbL-Assembled Bifunctional $(TPY_2Ru/nGO)_n$ Multilayer Thin-Film Electrodes for HER and OER in a Neutral Condition[a]

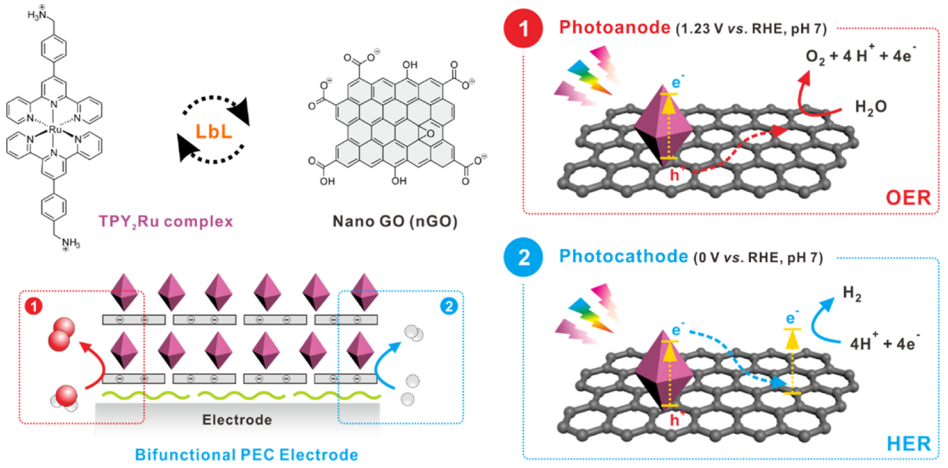

[a]The red and blue arrows indicate the hole and electron transfer pathways, respectively.

heterogenous photoelectrodes from the photocatalytic powder or dispersion.[20,21] Thus, the nanoscale controllable assembling of carbon nanomaterials for the successful development of efficient photoelectrodes and precise hybridization with other functional materials for facile charge transport are still required to resolve these problems.

In this regard, layer-by-layer (LbL) assembly can offer a versatile technique to fabricate the nanoscale thin-film electrode to integrate organic and inorganic nanomaterials.[22,23] Moreover, it can offer a means to design proper energy levels for effective Z-scheme and hybridize various nanomaterials for efficient PEC systems.[24−27] Specifically, the shifting and bending of band potentials in LbL-assembled electrodes can not only enhance the charge separation efficiency but also reduce the charge recombination for more efficient water splitting.[28] Although there have been some literature, including ours, reporting the LbL-assembled photosynthetic electrodes that integrate defective nanocarbons with other photoactive materials, the role of the nanocarbons was generally restricted to the facilitation of the electron transfer (see Table S1 in the Supporting Information).[29−33] In addition, their performance of photocurrent generation was still too low to meet any practical application and further study is needed to design the promising photocatalytic redox reaction (e.g., overall water splitting). The use of bifunctional photoelectrodes can thus lead to improved practical benefits; however, so far, only a limited number of studies have been reported on the bifunctionality of the photocatalytic LbL multilayer electrodes. Therefore, it is highly desirable to develop bifunctional photoelectrodes that combine both OER and HER under benign conditions for advanced PEC systems.

Here, we demonstrate a unique hybrid bifunctional multilayer photoelectrode composed of nanoscale graphene oxide (nGO) and a terpyridine complex of ruthenium(II) (TPY_2Ru) for overall water splitting reaction in benign conditions (Scheme 1). To construct an efficient PEC system for water splitting, we introduced a TPY_2Ru to harvest visible light to generate more photoinduced electrons[30,34] as well as nGO to provide photoactive sites for water splitting in the multilayer photoelectrode. The finely hybridized multilayer photoelectrode, using LbL assembly, combines the outstanding properties of each component and provides a synergistic effect for an efficient water splitting reaction. As a result, we achieved a significant photocurrent density with bifunctional photocatalytic activity in neutral pH, attributed to a highly enhanced charge transfer by effective energy level engineering for water splitting. Furthermore, this unique combination of soft components enables the development of a flexible thin-film photoelectrode. It exhibits a remarkable retention of current density of 1000 cycles in flexibility testing, which is otherwise challenging for other inorganic-based electrodes. We anticipate that this strategy can offer new insights into the facile nanoscale design of efficient hybrid photoelectrodes for future solar-fuel energy devices.

EXPERIMENTAL SECTION

Materials. All chemicals were purchased from Sigma-Aldrich unless otherwise noted. Potassium hydroxide, sodium hydroxide (Daejung Co., Ltd., Korea), and graphite nanofibers (Catalytic Materials, United States) were used without any further purification.

Preparation of nGO. nGO was synthesized from graphite nanofibers according to a literature method using a concentration of 0.50 mg/mL.[35,36]

Synthesis of TPY. An amine-functionalized terpyridine (TPY) ligand was synthesized from 2-acetylpyridine (Alfa Aesar, United States) and 4-cyanobenzaldehyde (Alfa Aesar, United States) using a previously reported protocol.[37]

Synthesis of the TPY_2Ru Complex. To prepare *cis*-dichloridotetrakis(dimethylsulfoxide) ruthenium(II) ($Ru(DMSO)_4Cl_2$), 2.0 g of $RuCl_3{\cdot}3H_2O$ (7.65 mmol) was dissolved in ethanol (50 mL).[38] The mixture was refluxed for 3 h, and the color of the solution changed from brown to deep green. After removing ethanol with a rotary evaporator, the remaining dark green residue was dissolved in dimethyl sulfoxide (DMSO) (8 mL). The solution was heated to 150 °C and stirred for 2 h with its color changing from green to bright orange. After cooling down to room temperature, the yellow solid product was precipitated and recrystallized by the addition of acetone (60 mL). The final yellow product, $Ru(DMSO)_4Cl_2$, was collected by filtration and washed with acetone. Finally, $Ru(DMSO)_4Cl_2$ (104.5 mg, 0.216 mmol) was added to 29.2 mL (0.432 mmol) of TPY solution dissolved in 0.10 M HCl and stirred at 80 °C for 24 h.

Fabrication of the LbL-Assembled Multilayer Electrode. Indium tin oxide (ITO)-coated glass substrates were cleaned by sonication in deionized (DI) water, acetone, and ethanol for 10 min each. Silicon and quartz substrates were cleaned by a piranha solution to remove any organic contamination and subsequently treated with

https://dx.doi.org/10.1021/acsaem.0c01154
ACS Appl. Energy Mater. XXXX, XXX, XXX−XXX

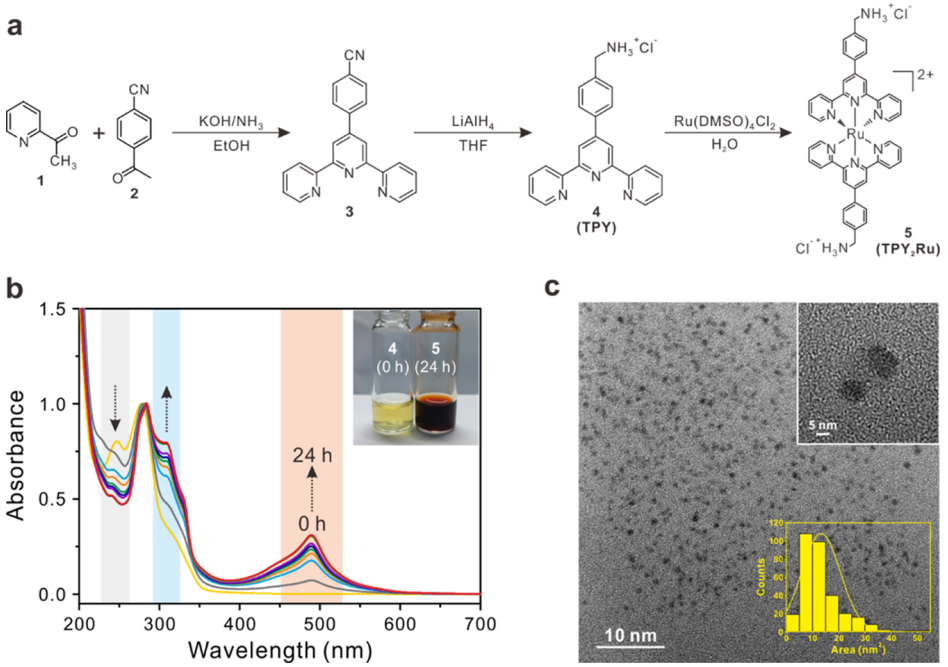

Figure 1. (a) Synthetic routes for the TPY_2Ru complex (**5**). (b) Changes in the UV/vis absorbance spectra from TPY to the TPY_2Ru complex with respect to the reaction time. The inset shows the corresponding solution color changes. (c) TEM images of nGO nanosheets with a lateral area distribution histogram counted over 100 samples.

poly(ethylene imine) (PEI) (Polymer Sciences, UK; M_w 10,000) to introduce a positively charged hydrophilic surface. These substrates were first dipped into a negatively charged nGO solution (0.50 mg/mL) at pH 3 for 10 min. They were then dipped into pH-adjusted DI water (pH 3) for 1 min three times to remove loosely bound nGO. Subsequently, the substrate was dipped into a positively charged TPY_2Ru complex suspension at pH 3 for 10 min and washed with pH-adjusted DI water (pH 3) three times for 1 min, which provided a one-bilayer film of $(TPY_2Ru/nGO)_1$. The above procedures were repeated to achieve the desired number of bilayers (BLs, n).

PEC Analysis. The as-assembled multilayer photoelectrodes were subjected to a thermal reduction process at 150 °C for 2 h in a tube furnace with an Ar atmosphere. The PEC performance was measured by linear sweep voltammetry (LSV) and chronoamperometry (CA) in the presence and absence of light irradiation using a WMPG 1000 multichannel potentiostat/galvanostat in 0.10 M potassium phosphate buffer solution at pH 7. A platinum planar and Ag/AgCl were used as a counter electrode and a reference electrode, respectively. For a general comparison, the potential of the Ag/AgCl reference electrode was converted to the potential of reversible hydrogen electrode (RHE) using $E_{RHE} = E_{Ag/AgCl} + 0.059 \cdot pH + E^{\circ}_{Ag/AgCl}$, where $E^{\circ}_{Ag/AgCl}$ = 0.1976 V at 25 °C. For a visible light source, a 300 W Xe lamp equipped with a 400 nm cut-on filter was employed. The gas evolution was quantified with a GC-2010 Plus gas Chromatograph (Shimadzu Co., Japan), and monitored during half-cell test in a customized 300 mL Pyrex glass container containing 60 mL of 0.10 M potassium phosphate buffer solution at pH 7 after argon purging for 30 min. For hydrogen evolution analysis, platinum was photo-deposited on the $(TPY_2Ru/nGO)_{30}$ multilayer film.[39,40] The multilayer electrode was dipped into 0.10 mM of hexachloroplatinic acid (H_2PtCl_6) aqueous solution containing 10% (v/v) of methanol sacrificial reagents. Then, the solution was degassed by N_2 for 30 min to avoid reoxidation and stirred for 1 h under visible light illumination (100 mW/cm^2). The Faradaic efficiency was determined using the following eq 1

$$\text{Faradaic efficiency (\%)} = \frac{z \times n \times F}{Q} \times 100 \quad (1)$$

where Q is the charge passed during the half-cell test for OER and HER, F is the Faraday constant, n is the number of moles of oxygen and hydrogen, and z is the number of electrons for OER and HER. Electrochemical impedance spectroscopy (EIS) was obtained in the range of 100 kHz to 0.1 Hz by a 1260 impedance analyzer (Solatron) at 1.41 V versus RHE for OER and 0 V versus RHE for HER under visible light irradiation.

Characterization. UV/vis spectroscopy (Shimadzu Co., UV-1800) characterized the absorbance of the thin films. Ellipsometry (J.A. Woollam Co. Inc., EC-400 and M-2000V) measured the thickness of the as-prepared samples on silicon substrates. A JEM 2100 (JEOL) captured the transmission electron microscopy (TEM) images in bright-field mode. An NX-10 atomic force microscope (Park Systems, Korea) was used to analyze the morphology and surface roughness. Thermogravimetric analysis (TGA, TA instruments, Q50) was used for the thermal properties of metal complex. A quartz crystal microbalance (QCM, Stanford Research System, QCM200) analyzed the active mass of each material adsorbed onto the film surface using the following Sauerbrey eqs 2 and 3

$$\Delta F\ (\text{Hz}) = -\frac{2F_o^2}{A\sqrt{\rho_q \mu_q}}\Delta m \quad (2)$$

$$\Delta F\ (\text{Hz}) = -56.6 \times \Delta m \quad (3)$$

where ΔF is the resonant frequency change (Hz), Δm is the mass change per unit area of the quartz crystal (μg/cm^2), F_o (5 MHz) is the fundamental resonance frequency of the crystal, A is the area of the Au−Cr electrode, ρ_q (2.65 g/cm^3) is the density of the quartz crystal, and μ_q (2.95 × 10^{11} g/cm·s^2) is the shear modulus. UV photoelectron spectroscopy (UPS) was carried out using an AXIS ultra-delay line detector (Kratos, UK) equipped with He I gas (21.22 eV) as a UV source.

RESULTS AND DISCUSSION

The highly stable aqueous TPY_2Ru complex and nGO dispersions are prerequisites for constructing LbL assemblies based on electrostatic interactions. The synthetic steps for the amine-functionalized TPY_2Ru complex are presented in Figure

https://dx.doi.org/10.1021/acsaem.0c01154
ACS Appl. Energy Mater. XXXX, XXX, XXX−XXX

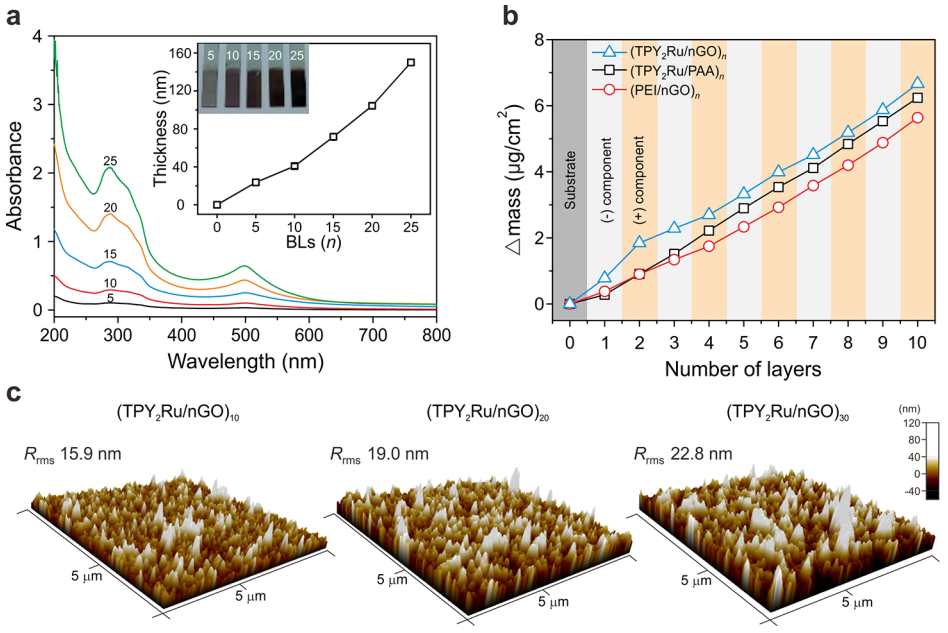

Figure 2. Characteristics of LbL-assembled multilayer photoelectrodes. (a) UV/vis absorbance spectra of a $(TPY_2Ru/nGO)_n$ multilayer film on quartz substrates. The inset shows the thickness of the $(TPY_2Ru/nGO)_n$ multilayer electrodes and the corresponding photographic images. (b) QCM analysis of the corresponding multilayer photoelectrodes as a function of the number of layers. (c) Representative AFM images of $(TPY_2Ru/nGO)_n$ (n = 10, 20, 30 from left to right) multilayer films on a silicon wafer with the corresponding R_{rms} values averaged over 10 μm × 10 μm.

1a. Initially, the TPY ligand was synthesized from the condensations of 2-acetylpyridine and 4-cyanobenzaldehyde, as confirmed by ^{1}H NMR (see Figure S1 in the Supporting Information). Subsequently, the TPY_2Ru complex was successfully prepared and characterized by UV/vis spectroscopy, ^{1}H NMR, and MALDI-TOF (Figures S2 and S3). UV/vis spectroscopy monitored the successful coordination between TPY and Ru(II), in which the clear development of a metal−ligand charge transfer (MLCT) band in the TPY_2Ru complex was observed at 489 nm with color changes from bright yellow to dark red (Figures 1b and S2a). With the progress of the MLCT band, $\pi-\pi^*$ transition of the TPY moiety at 247 and 310 nm was red-shifted because of the increased electron delocalization of the TPY moiety.[41] Moreover, ex situ ^{1}H NMR spectroscopy of the TPY moiety suggested the deshielding effect of electron delocalization upon complexation (Figure S2b). Meanwhile, TGA indicated that the as-synthesized TPY_2Ru complex displayed enhanced thermal stability as compared to the free TPY ligand up to 150 °C, at which temperature the electrodes were annealed in this study (Figure S4).

In parallel, the negatively charged colloidal suspension of nGO was prepared using graphite nanofibers according to the modified Hummers method. Instead of conventional GO, we choose nGO as it is known that nGO not only offers higher light harvesting because of the quantum confinement effect but also enhances electrocatalytic performance by enabling a facile mass transfer through increased diffusion pathways within the multilayer electrode.[35] TEM confirmed the successful synthesis of nGO with an average lateral size of 13.2 ± 7.4 nm^2 (averaged over 100 samples) (Figure 1c). Fourier transform infrared and X-ray photoelectron spectroscopy (XPS) further characterized nGO (Figure S5). The resulting stable aqueous suspensions of the TPY_2Ru complex and nGO displayed a high ζ-potential of +49.0 and −18.4 mV, respectively, at pH 3 for the LbL assembly (Figure S6a,b). In addition, the electrostatic interaction between nGO and the TPY_2Ru complex could be confirmed by immediate aggregation formed in a mixture of nGO and TPY_2Ru complex suspensions (Figure S6c).

With these stable suspensions of photoactive components, we fabricated the hybridized photoactive multilayer electrodes by LbL assembly, denoted as $(TPY_2Ru/nGO)_n$, where n = number of bilayers (BLs, typically n = 5−30). To investigate the synergistic coupling effect between TPY_2Ru and nGO, two control groups were also prepared; each photoactive material was used alone with other nonactive counterparts such as poly(acrylic acid) (PAA) and PEI to provide $(TPY_2Ru/PAA)_n$ and $(PEI/nGO)_n$ multilayer electrodes, respectively. To enhance the surface adhesion of the assembled multilayer, positively charged PEI was first deposited on the O_2-plasma-treated ITO substrate as a base layer. Additionally, this PEI layer reduces the work function of ITO substrates and improves the onset potential for water oxidation according to our previous studies.[28,42,43]

The successful growth of LbL-assembled multilayer electrodes was monitored by the gradual increase in absorbance in the UV/vis spectra (Figure 2a). The linear growth curve at 220 and 489 nm, corresponding to respective absorbance maxima of nGO and TPY_2Ru, clearly demonstrates the uniform multilayer formation after each deposition (Figures 2a and S7). The corresponding thickness of the $(TPY_2Ru/nGO)_n$ electrodes also showed a linear growth with respect to the number of deposition steps, with an average bilayer thickness of 6.0 nm.

The sequential adsorption of the TPY_2Ru and nGO was further analyzed using a QCM to quantify the amount of each component in the multilayer structure (Figure 2b). The relative mass ratio of the positive-to-negative components within each multilayer electrode was found to be 1.27, 1.06, and 1.18 for $(TPY_2Ru/PAA)_n$, $(PEI/nGO)_n$, and $(TPY_2Ru/nGO)_n$ multilayer electrodes, respectively. According to atomic force microscopy (AFM), the root-mean-squared roughness

https://dx.doi.org/10.1021/acsaem.0c01154
ACS Appl. Energy Mater. XXXX, XXX, XXX−XXX

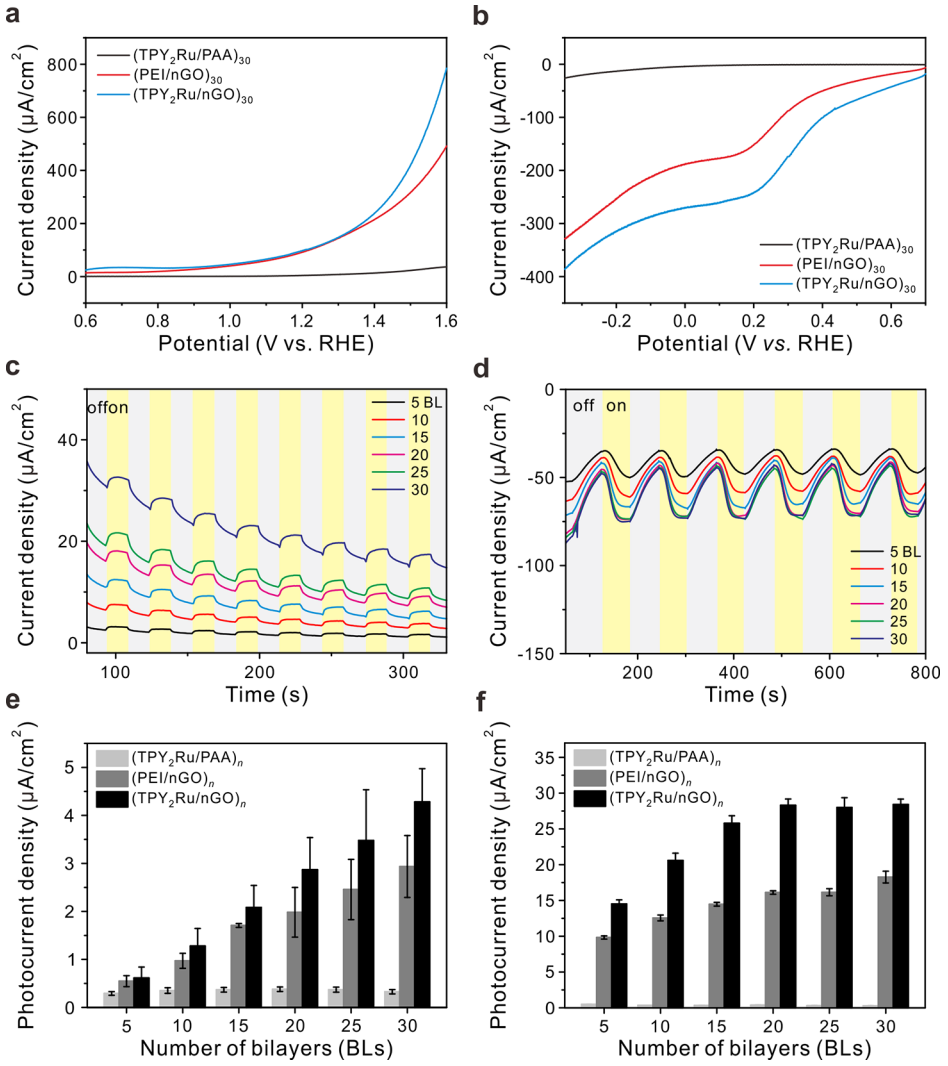

Figure 3. PEC performances of all types of multilayer photoelectrodes for OER and HER. (a,b) LSV of $(TPY_2Ru/nGO)_{30}$, $(TPY_2Ru/PAA)_{30}$, and $(PEI/nGO)_{30}$ multilayers: (a) photoanodes for OER and (b) photocathodes for HER under light irradiation. (c,d) CA of the $(TPY_2Ru/nGO)_n$ multilayer. (c) Photoanodes at 1.23 V vs RHE and (d) photocathodes at 0 V vs RHE as a function of the number of BLs under intermittent light. (e,f) Comparison of the photocurrent density for (e) OER and (f) HER with respect to the BLs. The photocurrent density was measured in five different points for each sample. All experiments were conducted in 0.1 M potassium phosphate buffer at pH 7.

(R_{rms}) of the $(TPY_2Ru/nGO)_n$ multilayer electrodes increased as a function of the number of BLs: 15.9 (10 BL), 19.0 (20 BL), and 22.8 nm (30 BL) (Figure 2c). This increment in surface roughness can be beneficial for enabling a facile mass transfer within diffusion-controlled 3D multilayer electrodes by increasing catalytic active sites, diffusion pathways, and interactions between the catalytic multilayer and the electrolyte, resulting in enhanced PEC performance.[35,44]

To evaluate the bifunctional activity of hierarchically assembled multilayer photoelectrodes for overall water splitting, LSV and CA were carried out in 0.10 M potassium phosphate buffer at pH 7 (Figure 3). First, the effect of thermal treatment on the performance of the $(TPY_2Ru/nGO)_{25}$ multilayer photoelectrode was investigated (Figure S8). A range of annealing temperatures were optimized from 100 to 200 °C based on the TGA of TPY_2Ru(II) (Figure S4). The photocurrent density increased after the annealing process at 150 °C, possibly because of the recovered structural integrity of the graphitic lattice (see XPS analysis in Figure S9), resulting in the enhancement of nGO conductivity, whereas the photocurrent density decreased after annealing at 200 °C because of the decomposition of the TPY complex, despite the enhanced nGO conductivity. This annealing effect was confirmed by the increased C/O ratio in the XPS analysis (Figure S9). For example, the C/O ratio of the as-prepared electrode was 4.18, which was then increased to 6.17 and 7.52 with increased annealing temperatures of 150 and 200 °C, respectively, indicating the successful thermal reduction in nGO at relatively low temperatures by decomposing oxygen-containing functional groups on nGO nanosheets such as carboxyl acid, hydroxyl, and epoxide groups.[45]

The current density of the $(TPY_2Ru/nGO)_{30}$ multilayer electrode was gradually increased with respect to the number of BLs under light irradiation as observed in the chronoamperogram (Figures 3 and S10). Interestingly, the PEC performance of the $(PEI/nGO)_n$ multilayer thin photoelectrodes was comparatively noticeable, demonstrating the photocatalytic activity of nanoscale nGO induced by the quantum-confinement effect. It was known that the quantized electronic structure of nGO led to a significant photocatalytic

https://dx.doi.org/10.1021/acsaem.0c01154
ACS Appl. Energy Mater. XXXX, XXX, XXX−XXX

activity.[46] To exclude the possibility of anodic photocurrent by oxidation of PEI, poly(diallyldimethylammonium chloride) (PDDA) was also employed in the multilayer electrode instead of PEI, which resulted in $(PDDA/nGO)_n$ (Figure S11). The photocurrent density of this control electrode was comparable to that of the $(PEI/nGO)_{30}$ electrode, verifying the photocatalytic activity of nGO itself within the multilayer electrode. The dark current density without light irradiation showed an increasing tendency with respect to the number of bilayers, which is attributed to the electrical double layer capacitance of nGO, including a modest faradaic capacitance of oxygen-containing functional groups on the surface of the nGO nanosheet.[47,48]

It is interesting to observe that the photocurrent density for OER was 4.28 $\mu A/cm^2$ in the $(TPY_2Ru/nGO)_{30}$ electrode, which was significantly higher than those of other control electrodes such as a simple mixture of TPY_2Ru and nGO (1.30 $\mu A/cm^2$), $(TPY_2Ru/PAA)_{30}$ (0.33 $\mu A/cm^2$), and $(PEI/nGO)_{30}$ (2.94 $\mu A/cm^2$), respectively, measured at 1.23 V (vs RHE) under visible light illumination (Figures 3c,e and S12). Under intermittent light irradiation, the upward and downward shape of the photocurrent density was observed, as shown in Figure 3c, which could originate from the effect of charge accumulation and dissipation within densely deposited multilayer electrodes.[49] Thus, the photoinduced electrons from TPY_2Ru can be accumulated at the interface of each layer, which have different transfer rates to the ITO substrate. After the lights were turned off, the accumulated electrons were slowly released, and this, in turn, resulted in a downward trend in photocurrent density. This accumulation effect was dominant in thicker electrodes (>20 BLs). In addition to photocatalytic activity, we also observed a slight cathodic shift (57.4 mV) of the onset potential from 5 to 30 BL for water oxidation (Figure S13).

In the case of the cathodic HER at 0 V (vs RHE), the photocurrent density in $(TPY_2Ru/nGO)_{30}$ electrodes under light irradiation was 28.42 $\mu A/cm^2$, which was much higher than those of other control electrodes such as a simple mixture of TPY_2Ru and nGO (8.88 $\mu A/cm^2$), $(TPY_2Ru/PAA)_{30}$ (0.29 $\mu A/cm^2$), and $(PEI/nGO)_{30}$ (18.27 $\mu A/cm^2$), respectively (Figures 3d,f and S12).

Additionally, in comparison with the simple sum of photocurrent values of $(TPY_2Ru/PAA)_{30}$ and $(PEI/nGO)_{30}$ for OER and HER (i.e., 3.27 $\mu A/cm^2$ at 1.23 V and 18.56 $\mu A/cm^2$ at 0 V, respectively), the hybridized $(TPY_2Ru/nGO)_{30}$ photoelectrode exhibited a much higher photocurrent density, at approximately 31 and 53% for OER at 1.23 V and HER at 0 V, respectively, outperforming many other metal-complex-based photocatalysts reported to date (Table S1). It should be highlighted that this synergistic effect of hybridization of TPY_2Ru and nGO on LbL-assembled electrodes is attributed to the bifunctional photocatalytic nGO with proper electronic structure and high density of photoexcited electrons that was achieved by a molecularly assembled LbL system with effective engineering of energy level for the overall water splitting reaction.

The kinetics and interfacial resistance in multilayer photoelectrodes were further evaluated by EIS at 1.41 V (vs RHE) for OER and 0 V (vs RHE) for HER (Figure S14). The charge-transfer resistance at the photocatalytic multilayer electrodes (R_{ct1}) and the photoelectrode/electrolyte interface (R_{ct2}) were obtained from the Nyquist plot, and the results are summarized in Table S2. It was found that both R_{ct1} and R_{ct2} of $(TPY_2Ru/nGO)_{30}$ multilayer electrodes were considerably smaller than those of $(PEI/nGO)_{30}$ and $(TPY_2Ru/PAA)_{30}$ for both OER and HER. These results verify that the photocatalytic activity of the bifunctional $(TPY_2Ru/nGO)_{30}$ photoelectrode was enhanced by facile charge transfer within the hybrid multilayer electrodes by directly coupling the photoactive TPY_2Ru and nGO without any nonactive counterparts.

To further elucidate the synergistic interplay by dual photoresponsive activities of nGO and the TPY_2Ru complex, we examined the position of the energy level of each component by UPS and Tauc plot analysis (Figure S15).[50] The band gap of nGO was determined as 2.60 eV, which is consistent with the band gap (2.50 eV) of a typical GO nanosheet.[17] On the other hand, the TPY_2Ru complex possesses a comparatively low band gap of 2.42 eV, which can provide large absorption of the visible light region in the multilayer photoelectrode to supplement the photoactivities of nGO. In addition, the ionization potential equivalent to the valence band energy of nGO and highest occupied molecular orbital level of TPY_2Ru was calculated to be 5.93 and 6.03 eV, respectively.[9,50] Based on these results, a schematic mechanism for effective Z-scheme with enhanced charge separation efficiency within the LbL-assembled photoelectrode is proposed in Figure 4. Specifically, with the assistance of the

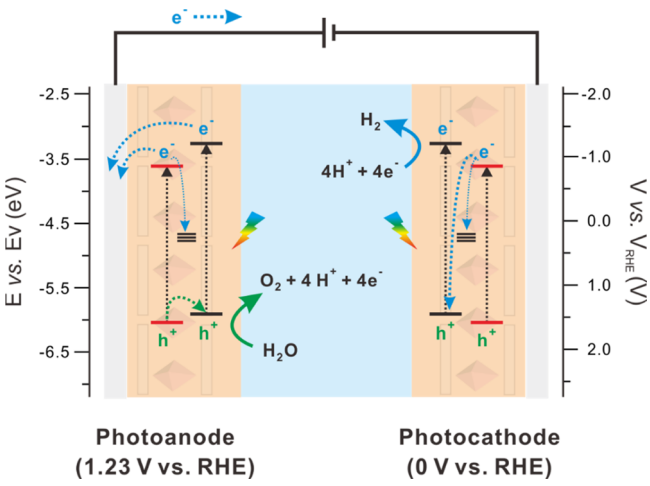

Figure 4. Proposed energy diagram and mechanism of hybrid bifunctional $(TPY_2Ru/nGO)_n$ multilayer electrodes for overall water splitting.

anodic bias, the separated holes were transferred to nGO for efficient charge separation and water oxidation reaction, establishing a heterostructure system within the hybrid multilayer electrode.[51] Meanwhile, an effective Z-scheme could be achieved between TPY_2Ru and nGO with ohmic contact, which resulted from multitudes of aggregated defects at the interface.[52] This ohmic contact made the energy level quasicontinuous for efficient usage of photogenerated electrons, namely, hydrogen reduction. Therefore, the interaction between two photocatalytic components in $(TPY_2Ru/nGO)_n$ electrodes engineered the positioning of the energy level with a suitable band gap for the bifunctional photocatalytic water splitting reaction.

To verify the photocatalytic bifunctionality for the overall water splitting reaction, gas production was monitored under light irradiation using gas chromatography (Figure 5a,b). Both

https://dx.doi.org/10.1021/acsaem.0c01154
ACS Appl. Energy Mater. XXXX, XXX, XXX−XXX

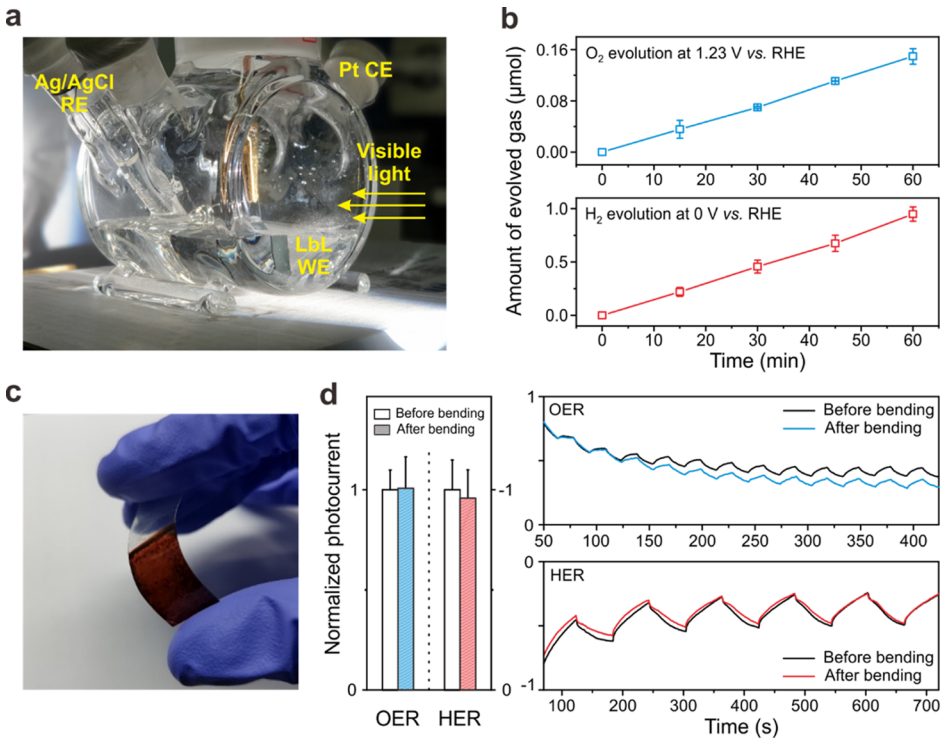

Figure 5. PEC performance of a $(TPY_2Ru/nGO)_{30}$ multilayer photoelectrode. (a) Photograph of the experimental setup for the gas evolution analysis in use. (b) Amount of the gas evolved from the $(TPY_2Ru/nGO)_{30}$ photoelectrode determined by gas chromatography. Note that the collected gas evolved from the respective OER and HER in each half-cell bifunctional electrodes operated under different potential biases (OER at 1.23 V and HER at 0 V vs RHE). (c) Photograph of a $(TPY_2Ru/nGO)_{30}$ multilayer electrode assembled on the ITO-coated PET substrate. (d) PEC performance of the flexible photoelectrocatalytic $(TPY_2Ru/nGO)_{30}$ multilayer electrode for bifunctional OER and HER after 1000 bending cycles (bending radius of 6.0 mm).

O_2 and H_2 were linearly produced with the progress of the respective reaction at an applied potential of 1.23 and 0 V versus RHE, respectively. In case of HER, Pt was employed as the cocatalyst because it was difficult to obtain a reliable quantification of H_2 because of the low detection limit (Figure S16). This linear increment of gas production proved the efficient bifunctional photocatalytic activities of alternatively hybridized $(TPY_2Ru/nGO)_n$ multilayer photoelectrodes for overall water splitting in benign conditions. The faradaic efficiency of the $(TPY_2Ru/nGO)_{30}$ photoelectrodes was determined during solar water splitting, resulting in 80.6 and 80.3% for OER and HER, respectively. The slight decrease from the ideal efficiency could be attributed to the photo-oxidation and reduction of nGO-based multilayer photoelectrodes, which was confirmed by measuring in nonaqueous electrolytes of acetonitrile containing 0.10 M tetrabutylammonium hexafluorophosphate ($TBAPF_6$) (Figure S17). It should also be noted that the generated O_2 and H_2 with photocurrent are originated from a solar water splitting reaction in the presence of water.

With the recent surge of interest in the development of flexible optoelectronic devices for practical applications in various fields such as rugged and collapsible electronics, and biomedical devices,[53,54] the superior flexibility and mechanical stability of the $(TPY_2Ru/nGO)_n$ multilayer electrodes were demonstrated, which are impossible to investigate in other conventional inorganic-based electrodes (Figure 5c,d). The bending durability test was performed for 1000 cycles at a bending radius of 6.0 mm, and a commercial ITO-coated PET film was used as a flexible conducting substrate. Figure 5d illustrates that the flexible photoelectrode exhibited remarkable durability without any damage to the films or a severe decrease (cycle retention of 100 and 96% for OER and HER, respectively) in its photocurrent density for 1000 bending cycles for both OER and HER. This outstanding mechanical flexibility is a result of not only the soft material properties but also the versatile LbL method enabling conformal deposition on any uneven substrate and assembling various nanomaterials at a molecular level into the hybrid multilayer films. Thus, these results demonstrate that the molecularly assembled LbL photocatalytic electrode can be further applied in PEC water splitting electrolyzers and flexible optoelectronic devices, which is challenging in other conventional inorganic electrodes.

■ CONCLUSIONS

A bifunctional photocatalytic multilayer electrode for water splitting, using a versatile LbL assembly, was fabricated. It was found that a hierarchically deposited multilayer electrode could provide significant advantages to improve the photocatalytic performance for the water splitting reaction by assembling the photocatalysts and photosensitizer elaborately and modulating the position of the energy level with a proper band gap. As a result, the LbL-assembled $(TPY_2Ru/nGO)_n$ multilayer thin-film electrodes showed bifunctional photocatalytic activity under benign conditions because of the synergistic coupling effect achieved by the hybridization of organic and inorganic nanomaterials. Furthermore, $(TPY_2Ru/nGO)_n$ multilayer photoelectrodes demonstrated remarkable flexibility and stability. We anticipate that this novel strategy can offer fascinating insights into energy level engineered designs of

https://dx.doi.org/10.1021/acsaem.0c01154
ACS Appl. Energy Mater. XXXX, XXX, XXX−XXX

highly versatile LbL photoelectrodes for future solar fuel energy and flexible devices.

■ ASSOCIATED CONTENT

Supporting Information

The Supporting Information is available free of charge at https://pubs.acs.org/doi/10.1021/acsaem.0c01154.

Previous literature for Ru complex-based photoelectrochemical cells non-assisted by photocatalytic metal oxide; ^{1}HNMR spectra of the TPY ligand and the TPY_2Ru complex; progress of TPY_2Ru complex formation; MALDI-TOF spectrum of the TPY_2Ru complex; TGA results of the TPY ligand and the TPY_2Ru complex; characterizations of nGO; ζ-potential of the TPY_2Ru complex and nGO; LbL growth curves of two control multilayer electrodes; PEC performance of the $(TPY_2Ru/nGO)_{25}$ multilayer film electrodes; characterizations of $(TPY_2Ru/nGO)_{30}$ multilayer electrodes; chronoamperometry data of different multilayer electrodes under different conditions; PEC performances of different multilayer thin films; Nyquist plots of EIS for three different multilayer electrodes; proposed two RC circuit models and fitting results of different Nyquist plots; band gap energy of nGO and TPY_2Ru; gas chromatography-based gas evolution of the $(TPY_2Ru/nGO)_{30}$ electrode; and comparison of current densities for $(TPY_2Ru/nGO)_{30}$ (PDF)

■ AUTHOR INFORMATION

Corresponding Authors

Minsu Gu − *Department of Chemistry, Yonsei University, Seoul 03722, Republic of Korea;* orcid.org/0000-0002-6270-7496; Email: sbgms@yonsei.ac.kr

Byeong-Su Kim − *Department of Chemistry, Yonsei University, Seoul 03722, Republic of Korea;* orcid.org/0000-0002-6419-3054; Email: bskim19@yonsei.ac.kr

Authors

Dongseok Kim − *Department of Chemistry, Yonsei University, Seoul 03722, Republic of Korea*

Yeongkyu Choi − *Department of Chemistry, Ulsan National Institute of Science and Technology (UNIST), Ulsan 44919, Republic of Korea;* orcid.org/0000-0001-5680-1390

Hyunwoo Kim − *Department of Energy Engineering and Emergent Hydrogen Technology R&D Center, Ulsan National Institute of Science and Technology (UNIST), Ulsan 44919, Republic of Korea;* orcid.org/0000-0002-1550-9745

Jungki Ryu − *Department of Energy Engineering and Emergent Hydrogen Technology R&D Center, Ulsan National Institute of Science and Technology (UNIST), Ulsan 44919, Republic of Korea;* orcid.org/0000-0002-0897-8463

Complete contact information is available at: https://pubs.acs.org/10.1021/acsaem.0c01154

Author Contributions

D.K. and M.G. contributed equally to this work. D.K. and M.G. contributed equally to the experimental work and conducted data analysis. M.G. and Y.C. participated in conceiving and designing the project. Y.C. assisted in the synthesis of the TPY complex. H.K. and J.R. assisted in the GC measurement. D.K., M.G., and B.-S.K. co-wrote the manuscript. All authors have given approval to the final version of the manuscript.

Notes

The authors declare no competing financial interest.

■ ACKNOWLEDGMENTS

This work was supported by the National Research Foundation of Korea (NRF) grant (NRF-2017M3A7B4052802). M.G. acknowledges the financial support from the Yonsei University Research Fund (2019-12-0131).

■ REFERENCES

(1) Schneider, J.; Matsuoka, M.; Takeuchi, M.; Zhang, J.; Horiuchi, Y.; Anpo, M.; Bahnemann, D. W. Understanding TiO2Photocatalysis: Mechanisms and Materials. *Chem. Rev.* **2014**, *114*, 9919−9986.

(2) Cook, T. R.; Dogutan, D. K.; Reece, S. Y.; Surendranath, Y.; Teets, T. S.; Nocera, D. G. Solar Energy Supply and Storage for the Legacy and Nonlegacy Worlds. *Chem. Rev.* **2010**, *110*, 6474−6502.

(3) Zhang, B.; Sun, L. Artificial Photosynthesis: Opportunities and Challenges of Molecular Catalysts. *Chem. Soc. Rev.* **2019**, *48*, 2216−2264.

(4) Xiao, F.-X.; Liu, B. Plasmon-Dictated Photo-Electrochemical Water Splitting for Solar-to-Chemical Energy Conversion: Current Status and Future Perspectives. *Adv. Mater. Interfaces* **2018**, *5*, 1701098.

(5) Sivula, K.; Le Formal, F.; Grätzel, M. Solar Water Splitting: Progress Using Hematite (α-Fe_2O_3) Photoelectrodes. *ChemSusChem* **2011**, *4*, 432−449.

(6) Roy, N.; Suzuki, N.; Terashima, C.; Fujishima, A. Recent Improvements in the Production of Solar Fuels: From CO_2 Reduction to Water Splitting and Artificial Photosynthesis. *Bull. Chem. Soc. Jpn.* **2019**, *92*, 178−192.

(7) Kim, J. H.; Hansora, D.; Sharma, P.; Jang, J.-W.; Lee, J. S. Toward Practical Solar Hydrogen Production − An Artificial Photosynthetic Leaf-to-Farm Challenge. *Chem. Soc. Rev.* **2019**, *48*, 1908−1971.

(8) Maeda, K.; Mallouk, T. E. Two-Dimensional Metal Oxide Nanosheets as Building Blocks for Artificial Photosynthetic Assemblies. *Bull. Chem. Soc. Jpn.* **2019**, *92*, 38−54.

(9) Liu, J.; Liu, Y.; Liu, N.; Han, Y.; Zhang, X.; Huang, H.; Lifshitz, Y.; Lee, S.-T.; Zhong, J.; Kang, Z. Metal-Free Efficient Photocatalyst for Stable Visible Water Splitting via a Two-Electron Pathway. *Science* **2015**, *347*, 970−974.

(10) Choi, S.; Nam, Y. S. Gold−Titanium Dioxide Half-Dome Heterostructures for Plasmonic Hydrogen Evolution. *ACS Appl. Energy Mater.* **2018**, *1*, 5169−5175.

(11) Kudo, A.; Miseki, Y. Heterogeneous Photocatalyst Materials for Water Splitting. *Chem. Soc. Rev.* **2009**, *38*, 253−278.

(12) Su, T.; Shao, Q.; Qin, Z.; Guo, Z.; Wu, Z. Role of Interfaces in Two-Dimensional Photocatalyst for Water Splitting. *ACS Catal.* **2018**, *8*, 2253−2276.

(13) Das, S. K.; Liu, Y.; Yeom, S.; Kim, D. Y.; Richards, C. I. Single-Particle Fluorescence Intensity Fluctuations of Carbon Nanodots. *Nano Lett.* **2014**, *14*, 620−625.

(14) Choi, Y.; Choi, Y.; Kwon, O.-H.; Kim, B.-S. Carbon Dots: Bottom-Up Syntheses, Properties, and Light-Harvesting Applications. *Chem.—Asian J.* **2018**, *13*, 586−598.

(15) Choi, Y.; Jeon, D.; Choi, Y.; Ryu, J.; Kim, B.-S. Self-Assembled Supramolecular Hybrid of Carbon Nanodots and Polyoxometalates for Visible-Light-Driven Water Oxidation. *ACS Appl. Mater. Interfaces* **2018**, *10*, 13434−13441.

(16) Yeh, T.-F.; Teng, C.-Y.; Chen, S.-J.; Teng, H. Nitrogen-Doped Graphene Oxide Quantum Dots as Photocatalysts for Overall Water-Splitting under Visible Light Illumination. *Adv. Mater.* **2014**, *26*, 3297−3303.

(17) Yeh, T.-F.; Chen, S.-J.; Yeh, C.-S.; Teng, H. Tuning the Electronic Structure of Graphite Oxide through Ammonia Treatment for Photocatalytic Generation of H_2 and O_2 from Water Splitting. *J. Phys. Chem. C* **2013**, *117*, 6516−6524.

(18) Samal, A.; Swain, S.; Satpati, B.; Das, D. P.; Mishra, B. K. 3D $Co_3(PO_4)_2$−Reduced Graphene Oxide Flowers for Photocatalytic Water Splitting: A Type II Staggered Heterojunction System. *ChemSusChem* **2016**, *9*, 3150−3160.
(19) Xiang, Q.; Yu, J. Graphene-Based Photocatalysts for Hydrogen Generation. *J. Phys. Chem. Lett.* **2013**, *4*, 753−759.
(20) Ryu, J.; Lee, E.; Lee, S.; Jang, J. Fabrication of Graphene Quantum Dot-Decorated Graphene Sheets via Chemical Surface Modification. *Chem. Commun.* **2014**, *50*, 15616−15618.
(21) Zhai, C.; Zhu, M.; Lu, Y.; Ren, F.; Wang, C.; Du, Y.; Yang, P. Reduced Graphene Oxide Modified Highly Ordered TiO_2 Nanotube Arrays Photoelectrode with Enhanced Photoelectrocatalytic Performance under Visible-Light Irradiation. *Phys. Chem. Chem. Phys.* **2014**, *16*, 14800−14807.
(22) Lee, S.; Song, Y.; Ko, Y.; Ko, Y.; Ko, J.; Kwon, C. H.; Huh, J.; Kim, S. W.; Yeom, B.; Cho, J. A Metal-Like Conductive Elastomer with a Hierarchical Wrinkled Structure. *Adv. Mater.* **2020**, *32*, 1906460.
(23) Ko, Y.; Shin, D.; Koo, B.; Woo Lee, S.; Yoon, W.-S.; Cho, J. Ultrathin Supercapacitor Electrodes with High Volumetric Capacitance and Stability using Direct Covalent-Bonding between Pseudocapacitive Nanoparticles and Conducting Materials. *Nano Energy* **2015**, *12*, 612−625.
(24) Jeon, D.; Kim, H.; Lee, C.; Han, Y.; Gu, M.; Kim, B.-S.; Ryu, J. Layer-by-Layer Assembly of Polyoxometalates for Photoelectrochemical (PEC) Water Splitting: Toward Modular PEC Devices. *ACS Appl. Mater. Interfaces* **2017**, *9*, 40151−40161.
(25) Kim, H.; Bae, S.; Jeon, D.; Ryu, J. Fully Solution-Processable Cu_2O−$BiVO_4$ Photoelectrochemical Cells for Bias-Free Solar Water Splitting. *Green Chem.* **2018**, *20*, 3732−3742.
(26) Kim, D.; Gu, M.; Park, M.; Kim, T.; Kim, B.-S. Layer-by-Layer Assembly for Photoelectrochemical Nanoarchitectonics. *Mol. Syst. Des. Eng.* **2019**, *4*, 65−77.
(27) Gross, M. A.; Creissen, C. E.; Orchard, K. L.; Reisner, E. Photoelectrochemical Hydrogen Production in Water using a Layer-by-Layer Assembly of a Ru dye and Ni Catalyst on NiO. *Chem. Sci.* **2016**, *7*, 5537−5546.
(28) Choi, Y.; Jeon, D.; Choi, Y.; Kim, D.; Kim, N.; Gu, M.; Bae, S.; Lee, T.; Lee, H.-W.; Kim, B.-S.; Ryu, J. Interface Engineering of Hematite with Nacre-like Catalytic Multilayers for Solar Water Oxidation. *ACS Nano* **2019**, *13*, 467−475.
(29) Jeong, D.-C.; Lee, J.; Lee, Y.; Satheeshkumar, C.; Song, C. Enhancement of Photoinduced Electron Transfer in Self-Assembled Polymer Films Using Mixed Metal−Terpyridine Complexes. *Macromolecules* **2015**, *48*, 1621−1626.
(30) Jeong, D.-C.; Song, S. G.; Satheeshkumar, C.; Lee, Y.; Kim, K.-s.; Song, C. Enhanced Photoinduced Electron Transfer by Multi-walled Carbon Nanotubes in Self-Assembled Terpyridine Polymer Networks. *Polymer* **2015**, *69*, 39−44.
(31) Meng, T.-T.; Zheng, Z.-B.; Wang, K.-Z. Layer-by-Layer Assembly of Graphene Oxide and a Ru(II) Complex and Significant Photocurrent Generation Properties. *Langmuir* **2013**, *29*, 14314−14320.
(32) Yang, W.; Zheng, Z.-B.; Meng, T.-T.; Wang, K.-Z. Synergistically Enhanced Photoelectrochemical Properties of a Layer-by-Layer Hybrid Film Based on Graphene Oxide and a Free Terpyridyl-Grafted Ruthenium Complex. *J. Mater. Chem. A* **2015**, *3*, 3441−3449.
(33) Ye, H.-Y.; Qi, J.-M.; Sun, R.; Gao, L.-H.; Wang, K.-Z. Photoelectric Active Hybrid Film Based on Ru^{II} Terpyridyl Complex and Eu^{III} Substituted Keggin Polyoxometalate of $[Eu(BW_{11}O_{39})_2]^{15-}$. *Electrochim. Acta* **2017**, *256*, 291−298.
(34) Song, S.; Xue, Y.; Feng, L.; Elbatal, H.; Wang, P.; Moorefield, C. N.; Newkome, G. R.; Dai, L. Reversible Self-Assembly of Terpyridine-Functionalized Graphene Oxide for Energy Conversion. *Angew. Chem., Int. Ed.* **2014**, *53*, 1415−1419.
(35) Gu, M.; Choi, J.; Lee, T.; Park, M.; Shin, I.-S.; Hong, J.; Lee, H.-W.; Kim, B.-S. Diffusion Controlled Multilayer Electrocatalysts via Graphene Oxide Nanosheets of Varying Sizes. *Nanoscale* **2018**, *10*, 16159−16168.
(36) Luo, J.; Cote, L. J.; Tung, V. C.; Tan, A. T. L.; Goins, P. E.; Wu, J.; Huang, J. Graphene Oxide Nanocolloids. *J. Am. Chem. Soc.* **2010**, *132*, 17667−17669.
(37) Kim, J.-H.; Gu, M.; Lee, D. H.; Kim, J.-H.; Oh, Y.-S.; Min, S. H.; Kim, B.-S.; Lee, S.-Y. Functionalized Nanocellulose-Integrated Heterolayered Nanomats toward Smart Battery Separators. *Nano Lett.* **2016**, *16*, 5533−5541.
(38) Brastos, I.; Alessio, E.; Ringenberg, M. E.; Rauchfuss, T. B. Ruthenium Complexes. In *Inorganic Synthesis*; Rauchfuss, T. B., Ed.; John Weiley & Sons, Inc.: Hoboken, NJ, 2010; Vol. 35, pp 148−163.
(39) Pan, Z.; Zhang, G.; Wang, X. Polymeric Carbon Nitride/Reduced Graphene Oxide/Fe_2O_3: All-Solid-State Z-Scheme System for Photocatalytic Overall Water Splitting. *Angew. Chem., Int. Ed.* **2019**, *58*, 7102−7106.
(40) Park, S.-Y.; Han, K.; O'Neill, D. B.; Mul, G. Stability of Ag@SiO_2 Core−Shell Particles in Conditions of Photocatalytic Overall Water-Splitting. *J. Energy Chem.* **2017**, *26*, 309−314.
(41) Bhaumik, C.; Das, S.; Maity, D.; Baitalik, S. A Terpyridyl-Imidazole (tpy-HImzPh_3) Based Bifunctional Receptor for Multichannel Detection of Fe^{2+} and F^- Ions. *Dalton Trans.* **2011**, *40*, 11795−11808.
(42) Zhou, Y.; Fuentes-Hernandez, C.; Shim, J.; Meyer, J.; Giordano, A. J.; Li, H.; Winget, P.; Papadopoulos, T.; Cheun, H.; Kim, J.; Fenoll, M.; Dindar, A.; Haske, W.; Najafabadi, E.; Khan, T. M.; Sojoudi, H.; Barlow, S.; Graham, S.; Bredas, J.-L.; Marder, S. R.; Kahn, A.; Kippelen, B. A Universal Method to Produce Low−Work Function Electrodes for Organic Electronics. *Science* **2012**, *336*, 327−332.
(43) Bae, S.; Kim, D.; Kim, H.; Gu, M.; Ryu, J.; Kim, B. S. Modulating Charge Separation Efficiency of Water Oxidation Photoanodes with Polyelectrolyte-Assembled Interfacial Dipole Layers. *Adv. Funct. Mater.* **2020**, *30*, 1908492.
(44) Gu, M.; Kim, B.-S. Unraveling the Importance of Controlled Architecture in Bimetallic Multilayer Electrode toward Efficient Electrocatalyst. *Nano Energy* **2016**, *30*, 658−666.
(45) Lipatov, A.; Guinel, M. J.-F.; Muratov, D. S.; Vanyushin, V. O.; Wilson, P. M.; Kolmakov, A.; Sinitskii, A. Low-Temperature Thermal Reduction of Graphene Oxide: In Situ Correlative Structural, Thermal Desorption, and Electrical Transport Measurements. *Appl. Phys. Lett.* **2018**, *112*, 053103.
(46) Li, L.; Wu, G.; Yang, G.; Peng, J.; Zhao, J.; Zhu, J.-J. Focusing on Luminescent Graphene Quantum Dots: Current Status and Future Perspectives. *Nanoscale* **2013**, *5*, 4015−4039.
(47) Jo, K.; Gu, M.; Kim, B.-S. Ultrathin Supercapacitor Electrode Based on Reduced Graphene Oxide Nanosheets Assembled with Photo-Cross-Linkable Polymer: Conversion of Electrochemical Kinetics in Ultrathin Films. *Chem. Mater.* **2015**, *27*, 7982−7989.
(48) Lin, Z.; Liu, Y.; Yao, Y.; Hildreth, O. J.; Li, Z.; Moon, K.; Wong, C.-p. Superior Capacitance of Functionalized Graphene. *J. Phys. Chem. C* **2011**, *115*, 7120−7125.
(49) Yu, H.; Bao, Z.; Oh, J. H. High-Performance Phototransistors Based on Single-Crystalline n-Channel Organic Nanowires and Photogenerated Charge-Carrier Behaviors. *Adv. Funct. Mater.* **2013**, *23*, 629−639.
(50) Nguyen, B.-S.; Xiao, Y.-K.; Shih, C.-Y.; Nguyen, V.-C.; Chou, W.-Y.; Teng, H. Electronic Structure Manipulation of Graphene Dots for Effective Hydrogen Evolution from Photocatalytic Water Decomposition. *Nanoscale* **2018**, *10*, 10721−10730.
(51) Wang, H.; Zhang, L.; Chen, Z.; Hu, J.; Li, S.; Wang, Z.; Liu, J.; Wang, X. Semiconductor Heterojunction Photocatalysts: Design, Construction, and Photocatalytic Performances. *Chem. Soc. Rev.* **2014**, *43*, 5234−5244.
(52) Huang, X.; Wang, J.; Li, T.; Wang, J.; Xu, M.; Yu, W.; El Abed, A.; Zhang, X. Review on Optofluidic Microreactors for Artificial Photosynthesis. *Beilstein J. Nanotechnol.* **2018**, *9*, 30−41.
(53) Lipomi, D. J.; Bao, Z. Stretchable, Elastic Materials and Devices for Solar Energy Conversion. *Energy Environ. Sci.* **2011**, *4*, 3314−3328.

https://dx.doi.org/10.1021/acsaem.0c01154
ACS Appl. Energy Mater. XXXX, XXX, XXX−XXX

(54) Varadhan, P.; Fu, H.-C.; Kao, Y.-C.; Horng, R.-H.; He, J.-H. An Efficient and Stable Photoelectrochemical System with 9% Solar-to-Hydrogen Conversion Efficiency via InGaP/GaAs Double Junction. *Nat. Commun.* **2019**, *10*, 5282.

NOTE ADDED AFTER ASAP PUBLICATION

This paper was originally published ASAP on July 15, 2020. Due to a production error, there was a mistake in the title. The corrected version was reposted on July 16, 2020.

https://dx.doi.org/10.1021/acsaem.0c01154
ACS Appl. Energy Mater. XXXX, XXX, XXX−XXX